Molecular mechanism for the subversion of the retromer coat by the *Legionella* effector RidL

Miguel Romano-Moreno[a], Adriana L. Rojas[a], Chad D. Williamson[b], David C. Gershlick[b], María Lucas[a], Michail N. Isupov[c], Juan S. Bonifacino[b], Matthias P. Machner[d,1], and Aitor Hierro[a,e,1]

[a]Structural Biology Unit, Centro de Investigación Cooperativa en Biociencias, 48160 Derio, Spain; [b]Cell Biology and Neurobiology Branch, Eunice Kennedy Shriver National Institute of Child Health and Human Development, National Institutes of Health, Bethesda, MD 20892; [c]The Henry Wellcome Building for Biocatalysis, Biosciences, University of Exeter, Exeter EX4 4SB, United Kingdom; [d]Division of Molecular and Cellular Biology, Eunice Kennedy Shriver National Institute of Child Health and Human Development, National Institutes of Health, Bethesda, MD 20892; and [e]IKERBASQUE, Basque Foundation for Science, 48011 Bilbao, Spain

Edited by Ralph R. Isberg, Howard Hughes Medical Institute and Tufts University School of Medicine, Boston, MA, and approved November 13, 2017 (received for review August 30, 2017)

Microbial pathogens employ sophisticated virulence strategies to cause infections in humans. The intracellular pathogen *Legionella pneumophila* encodes RidL to hijack the host scaffold protein VPS29, a component of retromer and retriever complexes critical for endosomal cargo recycling. Here, we determined the crystal structure of *L. pneumophila* RidL in complex with the human VPS29–VPS35 retromer subcomplex. A hairpin loop protruding from RidL inserts into a conserved pocket on VPS29 that is also used by cellular ligands, such as Tre-2/Bub2/Cdc16 domain family member 5 (TBC1D5) and VPS9-ankyrin repeat protein for VPS29 binding. Consistent with the idea of molecular mimicry in protein interactions, RidL outcompeted TBC1D5 for binding to VPS29. Furthermore, the interaction of RidL with retromer did not interfere with retromer dimerization but was essential for association of RidL with retromer-coated vacuolar and tubular endosomes. Our work thus provides structural and mechanistic evidence into how RidL is targeted to endosomal membranes.

pathogenic bacteria | membrane targeting | coat complex | *Legionella* effector | X-ray crystallography

Endosomal trafficking is a dynamic process by which cells modulate a wide array of physiological functions, including nutrient uptake, cellular polarization, cytokinesis, neural signaling, development, and the innate immune response (1, 2). Sorting of integral membrane proteins and associated macromolecules, termed "cargos," from endosomes requires complex molecular machineries that, through multiple protein–lipid and protein–protein interactions, bind to cargo and deform the membrane into a coated bud (3–5). Retromer is a coat complex that assembles on endosomes and forms tubular carriers for the delivery of recycled material to the plasma membrane, the *trans*-Golgi network, or other specialized organelles (6, 7). The retromer complex comprises a conserved VPS26–VPS29–VPS35 heterotrimer (with two VPS26 variants, VPS26A and VPS26B) that, in combination with various sorting nexin (SNX) proteins, is recruited to endosomal membranes to select cargo (8–10). The SNX family is a diverse group of proteins characterized by the presence of a phox homology domain that binds primarily to phosphatidylinositol 3-phosphate (PI3P) to target the proteins to the membrane (5, 11). Of the 33 SNXs described in mammals, 7 have been identified as putative retromer interactors: SNX1, SNX2, SNX5, SNX6, SNX27, SNX3, and SNX12. Retromer does not have intrinsic membrane-binding activity and thus relies on its association with SNXs, transmembrane cargo proteins, and the small GTPase Rab7 for recruitment to endosomes (12–15). Although the affinity of retromer for Rab7 is weak, simultaneous interactions with SNXs and cargo combined with retromer oligomerization most likely provide an avidity effect for a strong yet reversible interaction.

Other accessory proteins that directly interact with retromer and regulate endosomal trafficking include the FAM21 subunit of the WASH actin nucleation complex (16), the adaptor VPS9-ankyrin repeat protein (VARP) (17) that binds to the R-SNARE VAMP7 together with several Rab GTPases that function along distinct trafficking pathways (18), and the Tre-2/Bub2/Cdc16 domain family member 5 (TBC1D5), a GTPase-activating protein (GAP) that causes Rab7 inactivation and redistribution to the cytosol (14).

Recent biochemical and structural characterization of single subunits and subcomplexes from retromer have provided insights into its modular architecture and mechanisms of action. VPS35 adopts an elongated α-helical solenoid structure with some bending capability around the midsection, and functions as a platform on which VPS26 and VPS29 bind independently at opposite ends (19, 20). VPS26 adopts an arrestin-like fold (21, 22), interacts with the VPS35 N-terminal side, and—in complex with SNX3—functions as a cargo adaptor for the canonical recycling motif ØX(L/M) (where Ø is an aromatic amino acid) that mediates retromer-dependent sorting (20). In addition, association of Rab7 with the VPS35 N-terminal side enhances the interaction with cargo (15). VPS26 also interacts with the SNX27 PDZ domain for recruiting cargo proteins containing a type I PDZ domain-binding motif (23, 24). VPS29 has a metallophosphoesterase fold with two conserved surface patches at opposite sides (25, 26).

Significance

Deciphering microbial virulence mechanisms is of fundamental importance for the treatment of infectious diseases. *Legionella pneumophila*, the causative agent of Legionnaires' pneumonia, hijacks a variety of host cell factors during intracellular growth. Herein, we uncovered the molecular mechanism by which the *L. pneumophila* effector RidL targets the host VPS29, a scaffolding protein of endosome-associated sorting machineries. Using X-ray crystallography, we determined the structure of RidL, both alone and in complex with retromer. We found that RidL uses a hairpin loop similar to that present in cellular ligands to interact with retromer. This sophisticated molecular mimicry allows RidL to outcompete cellular ligands for retromer binding, explaining how *L. pneumophila* utilizes the endosomal sorting machinery to facilitate targeting of effector proteins.

Author contributions: J.S.B., M.P.M., and A.H. designed research; M.R.-M., A.L.R., C.D.W., D.C.G., M.L., M.N.I., and A.H. performed research; M.R.-M., A.L.R., C.D.W., D.C.G., M.L., M.N.I., J.S.B., M.P.M., and A.H. analyzed data; and M.R.-M., A.L.R., C.D.W., D.C.G., M.L., J.S.B., M.P.M., and A.H. wrote the paper.

The authors declare no conflict of interest.

This article is a PNAS Direct Submission.

Data deposition: The atomic coordinates and structure factors have been deposited in the Protein Data Bank, www.wwpdb.org (PDB ID codes 5OT4, 5OSH, and 5OSI).

[1]To whom correspondence may be addressed. Email: machnerm@mail.nih.gov or ahierro@cicbiogune.es.

This article contains supporting information online at www.pnas.org/lookup/suppl/doi:10.1073/pnas.1715361115/-/DCSupplemental.

The VPS35 C-terminal side interacts with the patch around the incomplete catalytic site of VPS29 and occludes it (19), whereas the opposite conserved patch interacts with two cysteine-rich zinc-binding motifs of VARP (17), and an extended loop (Ins1) from the TBC GAP domain of TBC1D5 ($TBC1D5_{TBC}$) (27). Thus, the VPS26 side of retromer contributes both directly and indirectly to cargo recognition and membrane docking in combination with different SNXs, whereas the VPS29 side functions as scaffold for dimerization and association with distinct accessory proteins that regulate retromer activity.

The exploitation of recycling endosomal transport by viral and bacterial pathogens is an emerging strategy used to evade degradation and to promote replication during infection (28). Given their biological importance and high level of conservation, it is not surprising that retromer and retromer-associated proteins are opportune targets of a variety of microbial proteins. Some examples include the envelope glycoprotein of the HIV type-1 that binds directly to retromer for endosome-to-Golgi transport (29), the capsid protein L2 of the human papillomavirus type 16 that binds to the PDZ domain of SNX27 for virion trafficking to the nucleus (30, 31), the tyrosine kinase-interacting (Tip) protein of the herpesvirus saimiri that interacts with the retromer subunit VPS35 to impair cation-independent mannose 6-phosphate receptor (CI-MPR) trafficking and down-regulate CD4 surface expression (32), and the effector IncE of *Chlamydia trachomatis* that binds to SNX5/6 and disrupts CI-MPR trafficking (33–35).

Another bacterium that hijacks host cell retromer function is *Legionella pneumophila*, the causative agent of Legionnaires' pneumonia. Upon phagocytosis by host cells, such as freshwater amoeba in the environment or alveolar macrophages during infection, the intravacuolar pathogen dictates the fate of the membrane compartment in which it resides (36). It inhibits fusion of the *Legionella*-containing vacuole (LCV) with endosomes and lysosomes (37), and instead promotes interaction with host vesicles from the early secretory pathway and other yet to be identified membrane compartments (38–40). In doing so, *L. pneumophila* creates a camouflaged intracellular replicative niche that supports its survival and replication (36). During infection, *L. pneumophila* delivers close to 300 proteins, called effectors, into the host cytosol via a specialized translocation apparatus termed the Dot/Icm type IV secretion system (T4SS) (41). The combined activity of these effectors subverts host processes and signaling pathways, including gene expression, metabolism, and vesicle trafficking to promote intracellular proliferation of *L. pneumophila* (42). Despite extensive efforts, most *L. pneumophila* effectors have not been characterized in detail and their mode of action has remained unknown.

RidL (Lpg2311/Ceg28) is a 1,167-amino acid protein that, like most *L. pneumophila* effectors, lacks sequence homology to known proteins (43). Recent studies revealed that RidL interacts with the VPS29 subunit of retromer, localizes to LCVs, and promotes intracellular replication of *L. pneumophila* within amoeba and macrophages (44). Considering that depletion of retromer components increases *L. pneumophila* growth, and ectopically produced RidL reduces retrograde trafficking, it was proposed that RidL might restrict retromer function (44). Nonetheless, despite the significance of the RidL–retromer interaction in bacterial infection, the molecular details and mechanistic implications remain unknown. In this work, we performed a comprehensive analysis of the RidL–retromer complex at a structural, molecular, and cellular level and discovered a remarkable mode of molecular mimicry used by RidL for specific subcellular membrane targeting through VPS29 interaction.

Results

The N-Terminal Region of RidL Mediates the Interaction with Retromer. The primary structure of RidL has no significant homology to other proteins that could facilitate the identification of functional domains. Thus, we performed experiments to identify the regions in RidL that are important for binding to retromer. Guided by secondary structure predictions, we created truncated forms of *ridL*, purified the corresponding proteins from *Escherichia coli*, and tested their ability to interact with retromer in pull-down assays. We found that only those fragments containing the N-terminal region spanning amino acids 30–236 interacted with a stable retromer subcomplex (VPS29–VPS35C) composed of VPS29 and the C-terminal region of VPS35 (amino acids 476–780) (Fig. 1 *A* and *B*). Fragments comprising the central ($RidL_{167–866}$) or C-terminal region ($RidL_{866–1167}$) of RidL, or GST alone (control), did not bind VPS29–VPS35C (Fig. 1*B*). Similar observations were made by size-exclusion chromatography (SEC), where full-length RidL or $RidL_{1–236}$ coeluted with retromer, the VPS29–VPS35C subcomplex, or monomeric VPS29, while the peak containing $RidL_{167–866}$ migrated separate from the peak of the VPS29–VPS35C subcomplex (Fig. S1). Since neither $RidL_{167–866}$ nor $RidL_{866–1167}$ showed any noticeable reduction in stability or solubility compared with RidL, it is unlikely that failure to bind VPS29 was due to their misfolding. Taken together, these analyses demonstrated that $RidL_{1–236}$ was the smallest fragment tested here that stably interacted with VPS29.

Next, we compared the binding affinity (K_d) of RidL with that of an N-terminal fragment (amino acids 30–236) of RidL ($RidL_{30–236}$) for retromer (VPS26–VPS29–VPS35) by isothermal titration calorimetry (ITC). We chose to use $RidL_{30–236}$ over $RidL_{1–236}$ for the ITC analysis because of better purification yields. The affinities of RidL (K_d = 151 nM) and $RidL_{30–236}$ (K_d = 164 nM) for retromer were similar, indicating that retromer binding was mediated mainly by the N-terminal region of RidL, and that no other region of RidL made a major contribution to complex formation (Fig. 1*C*). Furthermore, the affinities of RidL for either retromer, the VPS29–VPS35C subcomplex, or the monomeric VPS29 subunit were almost identical (K_d retromer = 151 nM; K_d VPS29–VPS35C = 151 nM; K_d VPS29 = 181 nM) (Fig. 1*D*), suggesting that binding of RidL to retromer occurred mainly, if not exclusively, through VPS29 independent of other retromer subunits. These results are fully consistent with the previously reported coimmunoprecipitation assays describing the VPS29–RidlL interaction (44), and further extend the precise mapping of $RidL_{30–236}$ as the region responsible for contacting the VPS29 subunit of retromer.

Structure of $RidL_{1–866}$. To further investigate the molecular basis for the binding of RidL to retromer, we initiated the structural characterization of the complex by X-ray crystallography. Initial attempts using either retromer, the VPS29–VPS35C subcomplex or the VPS29 subunit bound to different RidL constructs, yielded either no crystals or crystals with poor diffraction quality. The best crystals, obtained with the VPS29–VPS35C subcomplex and $RidL_{1–236}$, diffracted to 4.3 Å. At this stage, molecular replacement using the structure of the VPS29–VPS35C subcomplex (PDB ID code 2R17) provided a clear solution with four VPS35C–VPS29 molecules per asymmetric unit showing partial-difference electron density for $RidL_{1–236}$. However, the lack of high-resolution data precluded the iterative refinement and model-building steps necessary to extract structural information for $RidL_{1–236}$. Thus, we focused on obtaining a higher-resolution structure of uncomplexed RidL. The construct of RidL-encompassing amino acids 1–866 ($RidL_{1–866}$) produced well-diffracting crystals. The structure was solved by single-wavelength anomalous diffraction using selenium as the anomalous scatterer and refined to 3.0-Å resolution (Fig. 2*A*, Fig. S2 *A* and *B*, and Table S1).

The structure of $RidL_{1–866}$ corresponds to an all-α protein formed by 47 α-helices (Fig. 2 *A* and *B*). The overall structure adopts an S-shape with a length of 120 Å and a width of 50 Å at the top and 85 Å at the base (Fig. 2*A*). $RidL_{1–866}$ showed no obvious structural similarity to any known entry in the protein

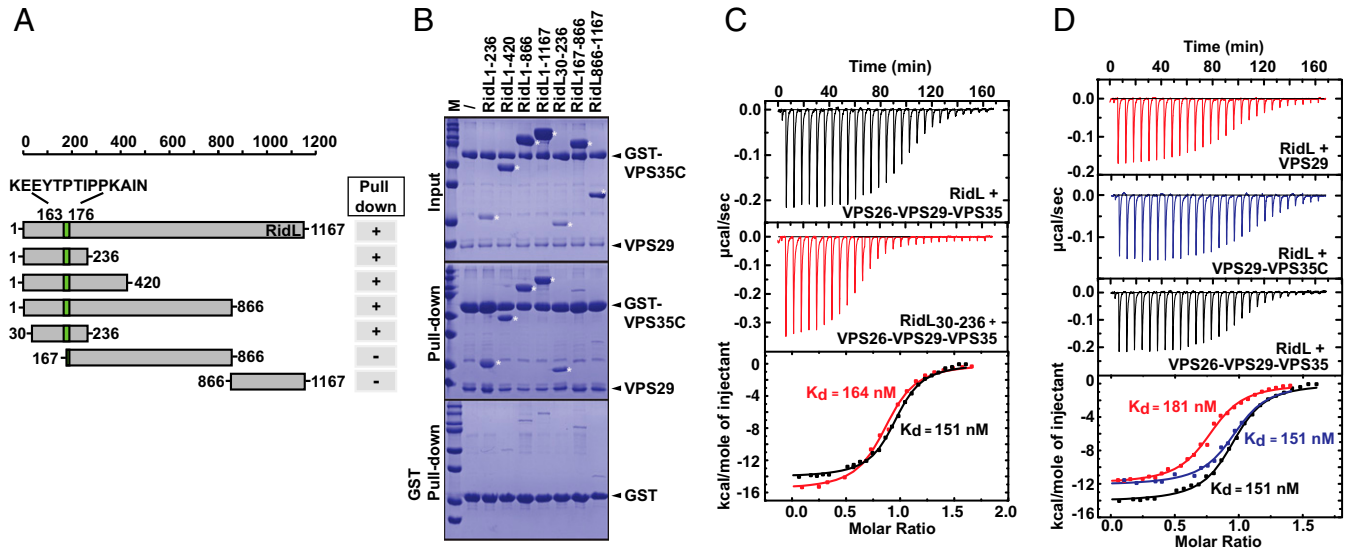

Fig. 1. The N-terminal region of RidL binds retromer through VPS29. (*A*) Schematic representation of the different constructs of RidL used in this work. The loop region of RidL involved in binding to retromer is colored in green. The plus (+) and minus (–) show whether the indicated constructs did or did not bind to VPS29–VPS35C. (*B*) Pull-down of RidL variants by VPS29-[GST-VPS35C] resolved by SDS/PAGE and visualized by Coomassie blue staining. The *Top* shows the protein input, while the *Middle* proteins bound to glutathione-Sepharose beads after incubation of VPS29-[GST-VPS35C] with each of the indicated RidL constructs. The *Bottom* shows a parallel pull-down using GST as bait that served as a negative control. Controls with GST-tag alone exhibit minimal nonspecific binding. M, molecular mass marker (250, 150, 100, 75, 50, 37, 25, and 20 kDa). The position of the respective proteins is indicated on the right. Bands corresponding to RidL constructs are marked with white asterisks (*). (*C*) ITC thermograms for the titration of RidL (black) or $RidL_{30–236}$ (red) with retromer. (*D*) ITC thermograms for the titration of RidL with VPS29 (red), VPS29–VPS35C (blue), and retromer (black). Thermodynamic binding parameters for ITC measurements in *C* and *D* are reported in Fig. S5C.

data bank [Dali server analysis (45)]. An alternative subdomain analysis also revealed no significant resemblance to other known domains except for the terminal three-helix bundle (amino acids 712–863) for which the sequence identity with the top matches was very low (less than 13%), thus limiting the prediction of potential functions for RidL (Fig. 2 *B* and *C*).

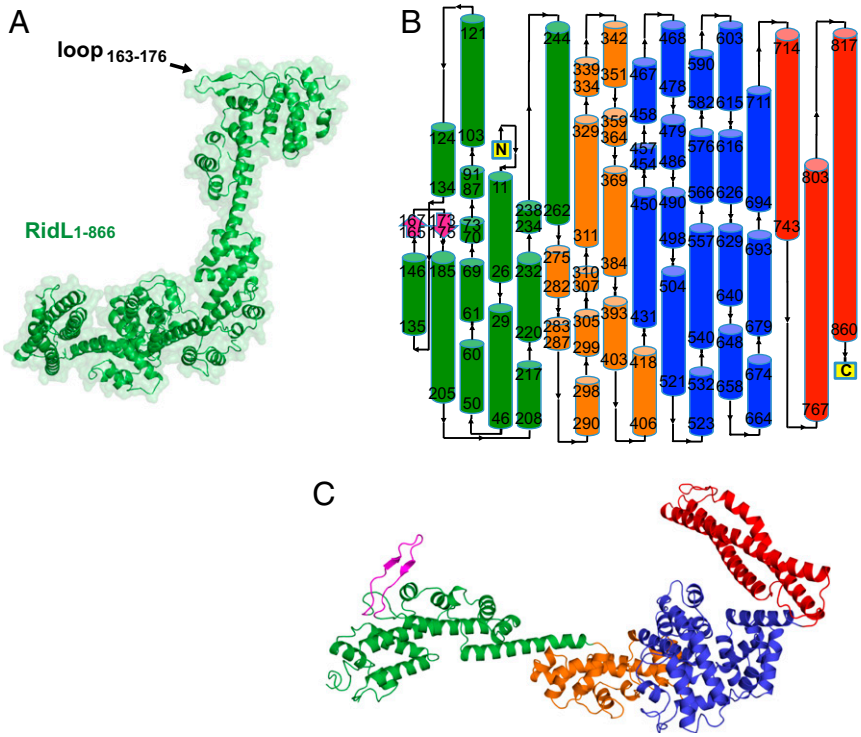

Fig. 2. Structure of $RidL_{1–866}$. (*A*) Overall structure of $RidL_{1–866}$ (green) represented by a ribbon diagram with transparent surface. The loop segment (residues 163–176) through which binding to VPS29 occurs is marked with an arrow. Topology diagram of $RidL_{1–866}$ (*B*) and ribbon diagram (*C*) colored on the basis of the different predicted domains: green (residues 6–262), orange (residues 263–429), blue (residues 430–711), red (residues 712–863), and magenta (residues 163–176).

Crystal Structure of RidL$_{1–236}$ Bound to the VPS29–VPS35C Subcomplex. With the 3.0-Å resolution structure of RidL$_{1–866}$ (Fig. 2) on hand, we used its RidL$_{1–236}$ part and the VPS35C–VPS29 structure (PDB ID code 2R17) as models for the molecular-replacement solution of the aforementioned 4.3-Å hetero-trimeric RidL$_{1–236}$–VPS29–VPS35C complex. The final structure has a free *R*-factor of 29.4 and good stereochemistry (Fig. S2 *C* and *D* and Table S1). The crystals contain four copies of each RidL$_{1–236}$ and VPS29–VPS35C in the asymmetric unit. Each RidL$_{1–236}$ molecule establishes contacts with two copies of VPS35C at different sites and a single contact with VPS29. The RidL$_{1–236}$–VPS29–VPS35C interaction occurs via a protruding hairpin loop of RidL (amino acids 163–176) that binds to a hydrophobic pocket on the surface of VPS29 opposite to the VPS29–VPS35C interface (Fig. 3*A*). Notably, no other region of RidL$_{1–236}$ establishes a direct contact with VPS29, suggesting that the interaction solely relies on the hairpin loop. Based on this observation, we crystallized a peptide comprising the entire hairpin loop (RidL$_{loop}$, residues $_{163}$KEEYTPTIPPKAIN$_{176}$) with VPS29–VPS35C, and determined the structure of the complex at 2.5-Å resolution (Fig. 3*B* and Table S1). The difference Fourier map shows clear electron density for the RidL peptide, with most side chains being well defined (Fig. S2 *E* and *F*). Overall, recognition of the hydrophobic pocket of VPS29 by RidL$_{loop}$ covers a surface area of 420 Å^2 and is dominated by hydrophobic interactions (Fig. 3 *C* and *D*). The side chains P168, I170, and P172 at the edge of the hairpin loop of RidL are the most-buried residues upon complex formation and are at the center of the interface. P168 interacts with a shallow hydrophobic pocket formed by L25, V172, and V174 of VPS29. The carbonyl group of the main chain of T169 establishes a hydrogen bond with Y165 of VPS29. The side chain of I170 inserts deep into a cavity formed by L2, L25, L26, K30, I31, L152, and Y165 of VPS29. The next residue in the hairpin loop, P171 further contributes to the burial of I170, making hydrophobic contacts with L2 and L152 of VPS29, while also helping to position the following P172 in a ring–ring stacking interaction with Y163 of VPS29. In addition, the interaction is reinforced with a hydrogen bond between Y166 of RidL and R176 of VPS29. More peripherally, Y166 of RidL is buried between the crossing segment of the hairpin loop and a shallow hydrophobic pocket formed by Y163, V174, and R176 of VPS29, thus providing an extended flat contact that further stabilizes the hairpin conformation. Importantly, a comparison between the primary sequences of VPS29 from human (the disease host) and other metazoa, including amoebae (the environmental host), showed that all VPS29 residues at the contact site are highly conserved (Fig. 3*E* and Fig. S3), suggesting that the interaction between RidL and VPS29 has the same binding mode in all hosts.

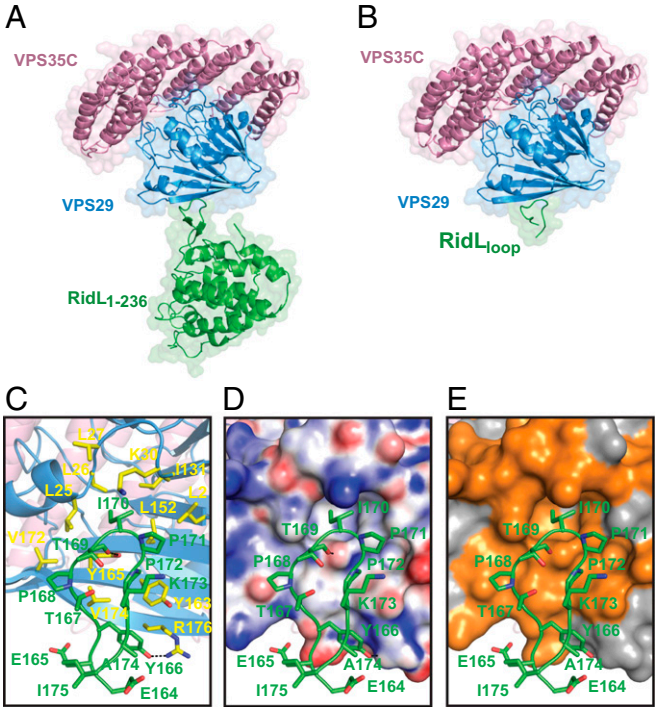

Fig. 3. Structures of RidL in complex with retromer. (*A*) Overall structure of the complex formed by RidL$_{1–236}$ and VPS29–VPS35C with transparent surfaces. RidL$_{1–236}$ is colored in green, VPS29 in blue, and VPS35C in pink. (*B*) Overall structure of VPS29–VPS35C in complex with the hairpin loop of RidL (residues 163–176) with transparent surface map. The structure is colored as in *A*. (*C*) VPS29–RidL$_{loop}$ interaction in detail. Critical VPS29 and RidL residues are shown as sticks. Hydrogen bonds formed between the RidL hairpin loop and VPS29 are denoted by black dashed lines. (*D*) Electrostatic surface potential (−25 to +25 kT/e in red to blue) mapped on the surface of VPS29 structure, in the same orientation as in *C*. (*E*) Strictly conserved residues shown in Fig. S3 are mapped onto the surface of VPS29.

Overall Assembly of the RidL–Retromer Complex in Solution. The structure of RidL$_{1–236}$ bound to the VPS29–VPS35C subcomplex presented here (Fig. 3) revealed two elongated macromolecules connected via a single-point junction. Interestingly, upon comparison of the structures of RidL$_{1–866}$ alone and RidL$_{1–236}$ bound to VPS29–VPS35C, it became clear that the orientation of the RidL hairpin loop involved in the interaction with VPS29 remained essentially unaltered, despite the different crystallization conditions and crystal packing interactions. To capture the global shape of the RidL–retromer complex, we performed small-angle X-ray scattering (SAXS) experiments and ab initio reconstructions. We obtained representative bead models with low average spatial discrepancy from two samples, RidL$_{1–866}$–VPS29–VPS35C and RidL$_{1–420}$–retromer (Fig. 4 *A* and *B* and Fig. S4 *A*–*D*). While the bead-model shape of RidL$_{1–866}$–VPS29–VPS35C was elongated and twisted with two protruding edges, the bead-model of RidL$_{1–420}$–retromer exhibited an elbow-shaped rod. Rigid-body refinement on the bead models using the crystal structures of RidL$_{1–866}$ (present study) and VPS29–VPS35C (19) (Fig. 4*A*), or RidL$_{1–420}$–VPS29–VPS35C (present study) and VPS26–VPS35N (20) (Fig. 4*B*) resulted in a very good fit between the theoretical scattering profiles for each macromolecular model and the experimental SAXS data (Fig. 4 *A* and *B* and Fig. S4 *A* and *B*). Superposition of both models yielded a complete RidL$_{1–866}$–retromer ensemble with a distinctive V-architecture (Fig. 4*C*). However, attempts to obtain a bead-model with RidL$_{1–866}$–retromer failed to converge on a single best-fit conformation, which might be indicative of a multiconformational equilibrium. In this scenario, the composite RidL$_{1–866}$–retromer ensemble would represent a conformational snapshot between fluctuating states.

Previous studies have demonstrated that retromer can form dimers through the VPS29 side ends at high protein concentration and physiological ionic strength (20, 46). Although the molecular details for the dimerization remain unknown, it has been speculated that the self-dimerization propensity could contribute to retromer coat assembly (20). Given that RidL interacted with retromer through the VPS29 subunit, we wondered whether RidL affects retromer dimerization. Using SEC with in-line multiangle light scattering (SEC-MALS), we characterized the molecular mass for each complex. Interestingly, RidL behaved as a monomer under physiological ionic strength, but when incubated with retromer, the complex exhibited a molar mass consistent with a 2:2 oligomer, thus allowing the formation of retromer dimers. In contrast, when RidL was incubated with monomeric retromer in a high ionic strength buffer, the molar mass was consistent with a 1:1 complex (Fig. S4 *E*–*G*).

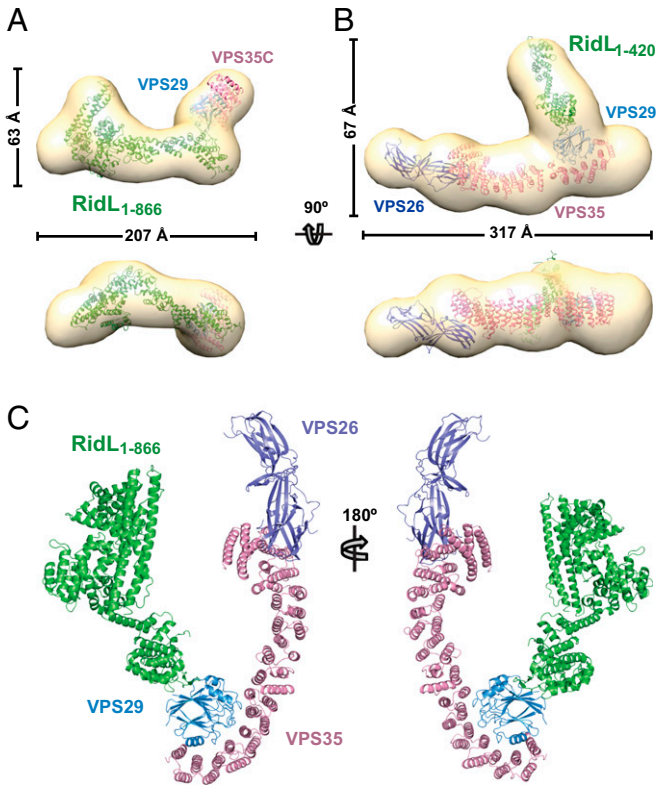

Fig. 4. Overall assembly of the RidL–retromer complex in solution. (*A* and *B*) Ab initio molecular envelopes generated from the SAXS scattering data of the $RidL_{1–866}$–VPS29–VPS35C complex (*A*) and $RidL_{1–420}$–retromer complex (*B*). The crystal structures of the individual domains are docked into the envelopes. (*C*) Proposed model of the $RidL_{1–866}$–retromer complex obtained from the superposition of $RidL_{1–866}$–VPS29–VPS35C and $RidL_{1–420}$–retromer complexes.

Therefore, the interaction of retromer with RidL did not preclude its dimerization in solution.

Mutations in the VPS29–RidL Interface Disrupt Complex Formation. To confirm that the binding mode between $RidL_{1–236}$ and VPS29–VPS35C observed in the crystal structure (Fig. 3) was responsible for complex formation in solution (Fig. 1), we introduced single-point mutations on contact site residues between VPS29 and RidL, and assessed their effect on protein interaction by pull-down as well as ITC measurements. We introduced the mutations L152E, Y163A, or Y165A within the central region of the VPS29 interface since those residues seemed especially important for binding to RidL. On the reciprocal side, we either replaced the central region of the hairpin loop (amino acids 166–173) of RidL, which protrudes into the conserved pocket of VPS29, by a single glycine linker ($RidL_{\Delta L}$), or introduced two single-point mutations Y166A and I170A. The overall secondary structure of these mutant proteins was not noticeably affected by the substitutions, as reflected by the fact that the circular dichroism spectra of the wild-type and mutant forms of RidL or VPS29 remained unchanged (Fig. S5 *A* and *B*). In agreement with the structural data, substitution of any of the interface residues strongly attenuated the interaction between VPS29 and RidL, as assessed by pull-down assays using GST-tagged RidL as bait (Fig. 5*A*). To corroborate these results, we determined the binding affinities of $VPS29_{L152E}$, $VPS29_{Y163A}$, $VPS29_{Y165A}$, $RidL_{\Delta L}$, $RidL_{Y166A}$, and $RidL_{I170A}$ using ITC (Fig. 5*B* and Fig. S5*C*). As expected, mutation of any of the interface residues (L152E, Y163A, Y165A in VPS29; Y166A, I170A in RidL), or truncation of the loop in RidL ($RidL_{\Delta L}$) resulted in a complete loss of binding, underscoring the critical importance of the hydrophobic and hydrogen bond interactions for the formation of a stable VPS29–RidL complex. We also evaluated the interaction between the synthetic $RidL_{loop}$ peptide (residues 163–176) and VPS29 but detected no binding by ITC, most likely because the peptide does not form the hairpin structure in solution that is critical for the recognition process. Finally, we tested the interaction between full-length RidL and the retromer complex containing either VPS29, $VPS29_{Y163A}$, or $VPS29_{Y165A}$ (Fig. 5*C* and Fig. S5*C*). Unlike wild-type retromer, retromer containing $VPS29_{Y163A}$ or $VPS29_{Y165A}$ failed to interact with RidL, further confirming that the crystal contacts observed between $RidL_{1–236}$ and VPS29–VPS35C are indeed relevant for complex formation between RidL and retromer.

RidL Localizes to Endosomal Membranes Occupied by Retromer. To assess if the interactions between RidL and retromer observed in vitro (Figs. 3 and 5) are also relevant in cells, we used fluorescence microscopy to examine the distribution of GFP-RidL–encoding constructs expressed by transient transfection in HeLa cells. Live-cell imaging of the transfected cells showed that the signal for full-length GFP-RidL was barely detectable. In contrast, a GFP-tagged, N-terminal RidL fragment comprising amino acids 1–236 (GFP-$RidL_{1–236}$) was produced at high levels and displayed a punctate cytoplasmic localization (Fig. 6*A*). Additional studies in fixed HeLa cells revealed that the cytoplasmic puncta containing GFP–$RidL_{1–236}$ colocalized with the endogenous VPS26 subunit of retromer (Fig. 6 *B* and *C*). Simultaneous production of either GFP- or mCherry-tagged $RidL_{1–236}$ with differently tagged forms of other organellar markers in live cells showed colocalization of $RidL_{1–236}$ with the VPS29 subunit of retromer (Fig. 6 *D* and *E*) and the endosomal proteins early endosome antigen 1 (EEA1), Rab5, and SNX12, but not the *trans*-Golgi network protein TGN38 (Fig. 6 *D* and *E* and Fig. S6*A*). Continuous live-cell imaging further revealed that mCherry-$RidL_{1–236}$ colocalized with YFP-VPS29 on vacuolar endosomes as well as dynamic tubules emanating from those endosomes (Fig. 6*D*, *Inset*, and Movie S1). EEA1-GFP also exhibited significant colocalization with mCherry-$RidL_{1–236}$ on the vacuolar part of endosomes but, unlike YFP-VPS29, it was not associated with the budding tubules (Fig. 6*D*, *Inset*, and Movie S2). Together, these studies demonstrated that exogenously produced $RidL_{1–236}$ specifically localized to vacuolar and tubular endosomes, and that the presence of RidL did not affect retromer localization to those membranous structures.

RidL Localization to Endosomes Requires VPS29 Binding. Our in vitro studies revealed that removal of the central region of the hairpin loop (amino acids 166–173) from RidL ($RidL_{\Delta L}$) abolished binding to either monomeric VPS29 or VPS29 as part of the retromer complex (Fig. 5). Hence, we tested if the hairpin loop played an equally important role for endosomal localization of RidL. Upon deletion of the hairpin loop in the context of GFP-$RidL_{1–236}$, the resulting GFP-tagged mutant protein (GFP-$RidL_{1–236,\ \Delta L}$) assumed a diffuse cytosolic distribution within cells, with no detectable enrichment on endosomal compartments (Fig. 6 *A–C* and *E* and Fig. S6 *B* and *C*). Failure to target to endosomes indicated that binding of RidL to retromer, in particular to VPS29, is essential for its proper localization within cells. To further test this hypothesis, we silenced retromer by RNA interference (RNAi), and analyzed its effect on RidL distribution. In contrast to mock RNAi-treated control cells, knockdown of the VPS35 subunit of retromer prevented association of GFP-$RidL_{1–236}$, but not EEA1, with endosomes (Fig. S7). Taken together, these experiments demonstrated that the interaction of the hairpin loop of RidL with retromer, revealed by our crystallographic and biochemical analyses, is essential for

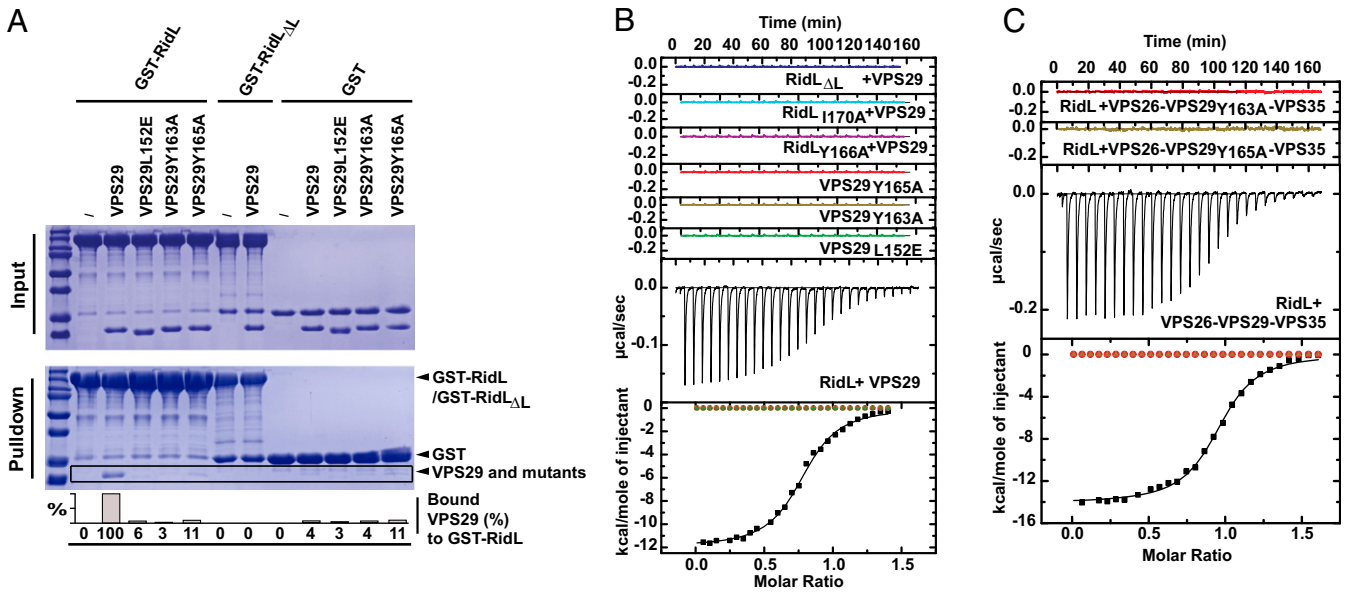

Fig. 5. Interface residues are critical for RidL–VPS29 complex formation. (*A*) Coomassie blue-stained SDS/PAGE gels showing pull-down of VPS29 wild-type or the different mutants of this protein by either GST-RidL, GST-RidL$_{\Delta L}$, or GST (control). Controls with GST-tag alone exhibit minimal nonspecific binding. The graph beneath the pull-down corresponds to densitometry-based quantification of the amount of VPS29 precipitated by the respective bait-coated beads. (*B*) ITC thermograms for the titration of RidL, RidL$_{\Delta L}$, or RidL point mutants (Y166A, I170D) into solutions containing either VPS29 or mutated versions of this protein. (*C*) ITC thermograms for the titration of RidL into solutions containing either retromer (black) and retromer containing VPS29$_{Y163A}$ (red) or retromer containing VPS29$_{Y165A}$ (brown).

association of RidL with retromer-coated vacuolar and tubular endosomes.

RidL Competes with Cellular Ligands for the Same Binding Site on VPS29. VPS29 contains two patches of conserved hydrophobic residues on opposite surfaces (25, 26). While one patch was reported to bind VPS35 (19, 25), the opposite patch mediates the association with the Rab7 GAP TBC1D5 (27) and the adaptor protein VARP (17). Interestingly, the pocket on VPS29 for binding TBC1D5 and VARP involves the same cluster of hydrophobic residues found here to interact with RidL (Figs. 3 and 5). Indeed, a comparison between the crystal structures of VPS29 in complex with a peptide derived from TBC1D5$_{TBC}$ (PDB ID code 5GTU) and the structure of VPS29 in complex with the hairpin loop of RidL (Fig. 3) revealed a common loop pattern with a conserved P-L/I motif as the linchpin of the interactions (residues I170-P171 in RidL; P141-L142 in TBC1D5) (Fig. 7*A*). Previously reported ITC titration assays of recombinant TBC1D5 $_{TBC}$ or VARP Cys-rich motifs to VPS29 yielded similar K_d values (5–13 μM) for both complexes in the low micromolar range, following a 1:1 stoichiometry (17, 27). As described above, RidL and RidL$_{1–236}$ exhibited a 1.5–2 log higher affinity for VPS29 and retromer (151 nM and 181 nM, respectively), which suggests that RidL could compete effectively against endogenous ligands. However, it has also been described that the association of TBC1D5$_{TBC}$ with retromer involves a binary interaction through both VPS29 and VPS35, with a K_d value of ∼220 nM (27) and, thus, closer to that observed herein for RidL binding to retromer (Fig. 1). Our ITC-derived K_d value for the interaction between TBC1D5$_{TBC}$ and retromer was comparable, although slightly higher, to those reported earlier (∼450 nM vs. ∼220 nM) (27), suggesting a weaker binding of TBC1D5 to retromer than RidL (Fig. S8 *A–D*).

To examine if RidL could compete with TBC1D5$_{TBC}$ for binding to retromer in solution, a preformed TBC1D5$_{TBC}$–retromer complex was incubated with an equimolar amount of RidL (Fig. 7 *B* and *D*), and the mixture was subsequently fractionated by SEC. In the absence of RidL, TBC1D5$_{TBC}$ and retromer migrated together, with enrichment in the fast-eluting fractions (10.5–12.5 mL). In contrast, upon addition of RidL, TBC1D5$_{TBC}$ was present almost exclusively in late-eluting fractions (14–15.5 mL), consistent with its displacement from retromer, while RidL coeluted with retromer (Fig. 7 *B* and *D*). Thus, under the conditions tested here, RidL outcompeted TBC1D5$_{TBC}$ for binding to retromer. Importantly, the mutant protein RidL$_{\Delta L}$ was unable to disrupt the preformed TBC1D5$_{TBC}$–retromer complex under the same conditions (Fig. 7 *B* and *D*), indicating that VPS29 binding was required for TBC1D5 displacement. In contrast, incubation of a preformed RidL–retromer complex with an equimolar amount of TBC1D5$_{TBC}$ did not result in the ejection of RidL from the retromer complex (Fig. S8 *E* and *F*), showing that RidL can resist displacement from VPS29 by cellular ligands.

To evaluate if RidL could compete with VARP in solution, we designed a VARP construct containing the two cysteine-rich domains involved in direct binding to VPS29 (VARPc, residues 396–746) and performed ITC and gel-filtration competition analysis. The ITC experiments showed that VARPc associates with retromer with a K_d of ∼3 μM and that two independent point mutations on VPS29 (Y165A and Y163A) completely abolished the interaction (Fig. S8 *C* and *D*). These results confirmed that VARP associates through the same VPS29 conserved pocket to retromer but with a weaker affinity than RidL. In addition, we analyzed the ability of RidL to displace VARPc from retromer by SEC. Due to the similar molecular weight between VARPc and the VPS26 subunit of retromer, we used a VPS29–VPS35 reconstituted retromer subcomplex to facilitate the visualization of proteins. As expected, RidL outcompeted VARPc for binding to VPS29–VPS35 but the mutant RidL$_{\Delta L}$ was unable to disrupt the preformed VARPc–VPS29–VPS35 complex (Fig. 7 *C* and *E*). In contrast, preformed RidL–VPS29–VPS35 complex was not outcompeted by VARPc under the same conditions (Fig. S8 *G* and *H*). These experimental results confirm that in solution RidL efficiently competed with VARP for binding to retromer.

We also examined if RidL could displace TBC1D5 from retromer in cells. In agreement with our biochemical experiments,

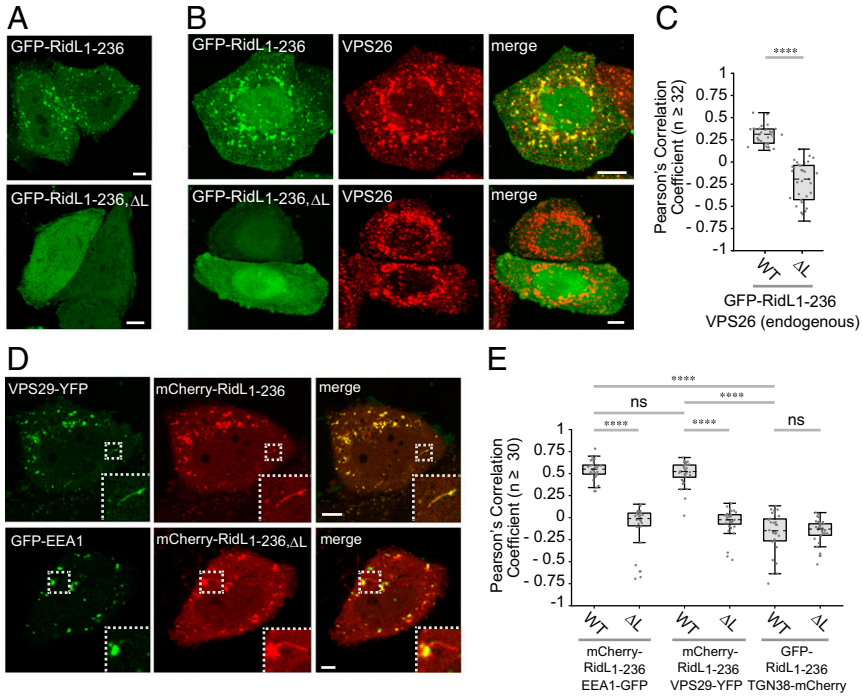

Fig. 6. RidL localizes to endosomal compartments occupied by retromer. (*A*) HeLa cells were transfected with plasmids encoding either GFP-RidL$_{1–236}$ or GFP-RidL$_{1–236,\Delta L}$ and imaged live 24 h later. (Scale bars, 5 μm.) (*B*) HeLa cells were transfected with plasmids encoding either GFP-RidL$_{1–236}$ or GFP-RidL$_{1–236,\Delta L}$ and fixed 24 h before staining with antibodies against the core retromer subunit VPS26. Notice the colocalization of GFP-RidL$_{1–236}$ with VPS26 on endosomal compartments. (Scale bars, 5 μm.) (*C*) Colocalization of GFP-RidL$_{1–236}$ or GFP-RidL$_{1–236,\Delta L}$ with endogenous VPS26 in fixed cells was quantified in at least 32 cells across three independent experiments using ImageJ. Pearson's correlation coefficient values for colocalization in individual cells are shown in the plots (****$P < 0.0001$ by unpaired *t* test with equal SD). (*D*) HeLa cells were cotransfected with plasmids encoding mCherry-RidL$_{1–236}$ and either YFP-VPS29 or early endosome marker EEA1-GFP, and imaged live. Still images were taken from Movies S1 (VPS29) and S2 (EEA1). (Scale bars, 5 μm.) *Insets* show mCherry-RidL$_{1–236}^{+}$ tubules (magnification: *Top*, 3.6×; *Bottom*, 2.5×). Notice the association of mCherry-RidL$_{1–236}$ with vacuolar endosomes labeled with YFP-VPS29 and EEA1-GFP, and emanating tubules labeled with YFP-VPS29 but not EEA1-GFP. (*E*) Colocalization of GFP-RidL$_{1–236}$ or GFP-RidL$_{1–236,\Delta L}$ with expressed EEA1-GFP, VPS29-YFP, or TGN38-mCherry in live cells was quantified in at least 30 cells across three independent experiments using ImageJ. Pearson's correlation coefficient values for colocalization in individual cells are shown in the scatter plots (****$P < 0.0001$, by unpaired *t* test with equal SD). ns, not significant.

overproduction of mCherry-RidL$_{1–236}$, but not mCherry-RidL$_{1–236,\Delta L}$, abrogated the association of GFP-TBC1D5 with endosomes (Fig. 7 *F* and *G*). These results demonstrated that RidL can effectively block a cellular ligand from binding to retromer, both in vitro and in vivo. We also observed weaker VARP-GFP fluorescence on endosomes from mCherry-RidL$_{1–236}$–overproducing cells relative to mCherry-RidL$_{236,\Delta L}$-overproducing cells (Fig. S9). However, a fraction of VARP-GFP remained associated with endosomes even in mCherry-RidL$_{1–236}$–overproducing cells (Fig. S9), suggesting that VARP has additional determinants for recruitment to endosomes.

Discussion

In this study, we have determined the structure of the *L. pneumophila* effector RidL, both alone and in complex with the human VPS29–VPS35C retromer subcomplex, and deciphered the molecular mechanism by which RidL is targeted to endosomal membranes. The crystal structure of RidL$_{1–866}$ is comprised of four domains that show neither sequence nor structural homology to other proteins. Targeting of RidL to recycling endosomes was solely dependent on a hairpin loop (amino acids 163–176) that binds to a conserved patch of exposed hydrophobic residues on VPS29. Interestingly, the binding mode of RidL with VPS29 was remarkably similar to that of the endogenous factor TBC1D5 (27). Indeed, TBC1D5 and VARP use the same binding patch on VPS29 for their association with retromer (17, 27) but bind with lower affinities compared with RidL. Consistent with these results, RidL effectively competed with TBC1D5 for binding to retromer in vitro and in vitro. RidL also outcompeted VARPc for binding to retromer in vitro, but only partially displaced VARP from endosomes in vivo (Fig. 7 and Fig. S9). This latter observation suggests that VARP has additional means of association with endosomes.

TBC1D5 possesses GAP activity toward Rab7, which has been proposed to promote retromer disassociation from membranes (14). During nutrient starvation, TBC1D5 can also associate with LC3, a protein involved in autophagy, which shuttles it away from its inhibitory interaction with retromer to promote GLUT1 recycling to the plasma membrane (47). These observations are evidence that the binding site on VPS29 may serve as a switch between mutually exclusive interactions to enhance or restrict retromer function within particular trafficking pathways. Furthermore, the recent identification of retriever, a related heterotrimer that shares the VPS29 subunit but recycles different cargoes, provides an even larger diversity of sorting events dependent upon VPS29 (48). Interestingly, endogenous retromer and retriever overlap on the same subdomains of endosomal membranes (48), so it is possible that RidL recruitment to these subdomains could also involve retriever. Our study suggests that RidL exploits the conserved pocket on VPS29 through molecular mimicry to efficiently reach specific endosomal subdomains where various cargo-retrieval machineries are located.

Recent studies have shown that *L. pneumophila* mutants lacking *ridL* exhibit a mild growth defect in the amoebean host *Dictyostelium discoideum* as well as in mouse RAW264.7 macrophages, while depletion of some (VPS26A/B, VPS29) but not all retromer subunits by RNA interference caused a subtle stimulation in *L. pneumophila* growth in HeLa cells (44). Similarly, ectopic production of RidL in HeLa cells or infection of

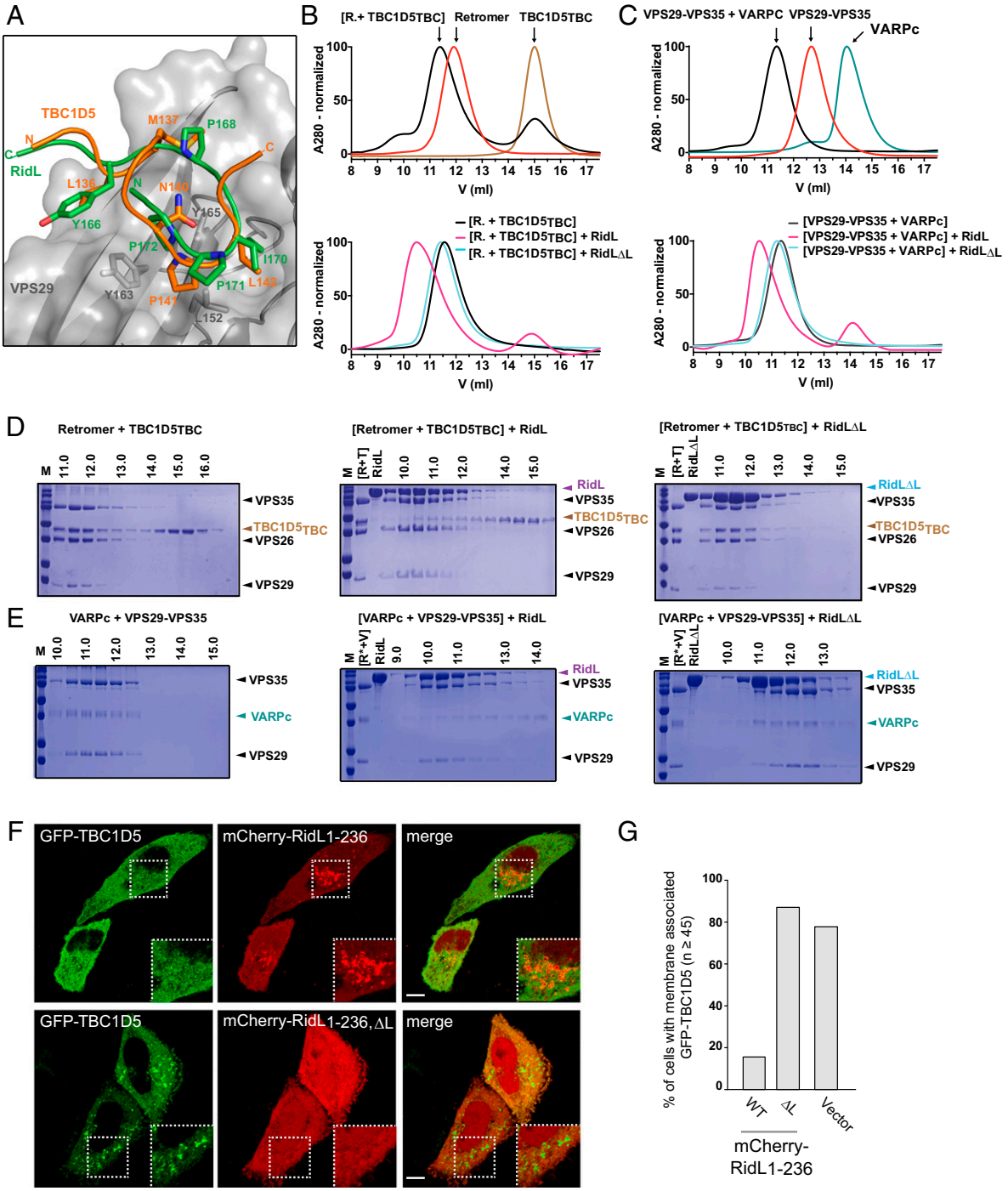

Fig. 7. RidL competes with TBC1D5$_{TBC}$ for binding to retromer. (*A*) Superposition of the VPS29/TBC1D5–Ins1 complex (PDB ID code 5GTU) shown in orange and the VPS29–VPS35–RidL$_{loop}$ complex (green). (*B*, *Upper*) Gel-filtration chromatogram of the complex formed by retromer and TBC1D5$_{TBC}$ (black) at a molar ratio of 1:1.5. The chromatograms of retromer (red) and TBC1D5$_{TBC}$ (brown) are also shown. (*Lower*) Competition assay between RidL and TBC1D5 for retromer binding. Gel-filtration chromatogram of the complex formed by retromer and TBC1D5$_{TBC}$ (black), after incubation with RidL at a 1:1 molar ratio (magenta) and after the incubation with RidL$_{\Delta L}$ (cyan). (*C*, *Upper*) Gel-filtration chromatogram of the complex formed by VPS29–VPS35 and VARPc (black) at 1:1 molar ratio. The chromatograms of VPS29–VPS35 (red) and VARPc (green) are also shown. (*Lower*) Competition assay between RidL and VARPc for retromer binding. Gel-filtration chromatogram of the complex formed by VPS29–VPS35 and VARPc (black), after incubation with RidL (magenta) and after the incubation with RidL$_{\Delta L}$ (cyan). (*D* and *E*) Coomassie blue-stained SDS/PAGE gels of the corresponding fractions shown in the chromatograms, with the position of each protein band indicated on the right. Gels with the corresponding fractions of the competition assays between RidL and RidL$_{\Delta L}$ are shown in the *Center* and on the *Right*, respectively. (*F*) Overproduction of mCherry-RidL$_{1–236}$ but not mCherry-RidL$_{1–236,\Delta L}$ displaces GFP-TBC1D5 from endosomes. HeLa cells were cotransfected with plasmids encoding GFP-TBC1D5 and either mCherry-RidL$_{1–236}$ or mCherry-RidL$_{1–236,\Delta L}$, and imaged live after 24 h. *Inset* shows endosomal recruitment of either mCherry-RidL$_{1–236}$ or GFP-TBC1D5 in representative images of three independent repeats (magnification: *Top*, 1.8×, *Bottom*, 1.6×). (Scale bars, 5 μm.) (*G*) A minimum of 45 cells coexpressing GFP-TBC1D5 and either mCherry-RidL$_{1–236}$, mCherry-RidL$_{1–236,\Delta L}$, or mCherry vector were assessed for association of GFP-TBC1D5 signal with intracellular membranes. Bar graphs report percentage of the cell population displaying membrane-associated GFP-TBC1D5 for each condition in a single matched experiment.

macrophages by wild-type *L. pneumophila* but not *L. pneumophila* mutants lacking RidL inhibited retrograde trafficking of subunit B from Shiga toxin or cholera toxin, two well-established model cargos for analyzing retromer-dependent retrograde transport (44). These data hint at a role for retromer in restricting *L. pneumophila* proliferation, and that RidL is translocated by *L. pneumophila* to counteract retromer function (44). However, some of the findings presented here argue that RidL has a more nuanced effect on retromer function. For example, although high levels of RidL compete with cellular ligands, such as TBC1D5, for VPS29 binding in transiently transfected HeLa cells (Fig. 7), the number of RidL molecules translocated by a single *L. pneumophila* bacterium into infected host cells is likely orders-of-magnitude lower than the copy number of retromer molecules, making it improbable that competitive binding to VPS29, which is an abundant protein present in at least two endosomal complexes, will cause a global collapse of endosomal recycling within cells. In addition, our SEC-MALS analyses demonstrated that $RidL_{1–866}$ binding to retromer did not preclude retromer dimerization (Fig. S4), a process that has been speculated to contribute to coat assembly (20), suggesting that retromer might still be able to assemble into a coat-like lattice on recycling endosomal tubules even in complex with RidL. Furthermore, the presence of exogenous RidL did not disturb the localization of retromer subunits to endosomal membranes or the formation of tubular structures emanating from those compartments (Fig. 6), suggesting that retrograde transport proceeded normally even in the presence of RidL. Thus, our findings support a VPS29-dependent membrane targeting mechanism rather than a widespread inhibitory activity.

Retromer and retriever have been predicted to share similar architecture and to spatially overlap in endosomal subdomains despite interacting with different combinations of SNX proteins for their association with membranes (48). RidL and the SNXs linked to retromer and retriever are PI3P-binding proteins. We have not found structural evidence of a PI3P-binding site in $RidL_{1–866}$. Despite extensive cocrystallization experiments of $RidL_{1–866}$ with PI3P analogs, we were unable to identify any extra density associated with the protein, possibly due to steric occlusion in the crystal packing, ionic strength in the crystallization solution, or because PI3P binds to the unsolved C-terminal region of RidL (residues 867–1167). Nonetheless, phosphoinositide-binding domains are usually complemented by other protein-binding domains to integrate the simultaneous binding of multiple factors in the same membrane. This sort of coincidence detection can facilitate submembrane localization, increase the apparent affinity due to the avidity effect or trigger a cellular process as part of a multivalent interaction (49).

At this time, we can only speculate about the function of RidL during *L. pneumophila* infection. RidL is a large effector composed of multiple domains with very low structural similarity to other known proteins; thus, it is probable that concomitant interactions with VPS29 and other, yet unidentified, factors could direct RidL specifically and efficiently to the LCV to interfere with lysosome fusion. This is consistent with the observation that VPS29 localizes to LCVs in a Dot/Icm-dependent, but RidL-independent manner and that LCVs formed by ΔridL accumulated more lysosome-associated membrane protein 1 (44). Interestingly, in yeast, the release of the Rab-like Rab7/Ypt7 from retromer favors the interaction with the HOPS tethering complex, which in turn promotes SNARE-dependent fusion of the late endosome with vacuoles (50). Thus, it is conceivable that RidL could prevent Rab7 disociation from retromer by displacing TBC1D5 to restrain the interaction with the mammalian HOPS–RILP tethering complex (51) and ultimately impede the fusion with lysosomes.

In conclusion, our results have shown that RidL interacts with VPS29 through a hairpin loop closely mimicking the natural TBC1D5 interaction and that this binding targets RidL to sites where retromer is present, most probably outcompeting cellular ligands. These findings mechanistically explain the targeting of RidL to subcellular membrane domains and pave the way for future research to define the ultimate function of RidL during *L. pneumophila* infection.

Materials and Methods

Recombinant Protein Production. The different constructs encoding RidL (RidL, $RidL_{30–236}$, $RidL_{1–236}$, $RidL_{1–420}$, $RidL_{1–866}$, $RidL_{866–1167}$, $RidL_{\Delta L}$, $RidL_{Y166A}$, $RidL_{I170D}$), human VPS29 and VPS29 mutants ($VPS29_{Y165A}$, $VPS29_{Y163}$, $VPS29_{L152E}$), and VARPc (residues 396–746) were cloned into the vector pGST-Parallel2 (52) using restrictions enzymes and Gibson assembly. $VPS29_{Y163A}$ and $VPS29_{Y165A}$ were also cloned into pmr101A (American Type Culture Collection) to form the mutated retromer complex. DNA encoding human $TBC1D5_{TBC}$ (residues 1–419) was cloned into the pDB-HisGST vector (DNASU; ID: EvNO00085134). Production of native proteins was performed in *E. coli* BL21(DE3), whereas proteins labeled with Seleno-L-methionine (SeMet) were isolated from *E. coli* B834(DE3), as described previously (20).

Protein Crystallization and Structure Determination. Crystals were grown by hanging-drop vapor diffusion at 18 °C. Native and SeMet derivative crystals of $RidL_{1–866}$ were obtained by mixing 1 μL of 100–120 μM protein with 1 μL of well solution containing 0.4 M sodium fluoride, 14–16% (wt/vol) polyethylene glycol (PEG) 3350, and 0.1 M Bis·Tris propane pH 7.5. The crystallization of native and SeMet-labeled complexes of $RidL_{1–236}$–VPS29–VPS35C was achieved by mixing 1 μL of the purified complex at 7.5 mg/mL and 1 μL of the precipitant solution containing 0.1 M sodium chloride, 0.1 M Tris pH 8.0 and 4–8% (vol/vol) PEG6000. The $RidL_{1–866}$ structure was solved using experimental (SeMet SAD) phasing followed by density modification. The structure of the $RidL_{1–236}$–VPS29–VPS35C complex was solved by molecular replacement combined with SAD phases (SAD-MR) using the known structure of VPS29–VPS35C complex (PDB ID code 2R17) and the anomalous signal of two crystals; one in which the VPS29–VPS35 subcomplex was labeled with SeMet, and the second in which only $RidL_{1–236}$ was labeled with SeMet. VPS29–VPS35C–$RidL_{loop}$ was solved by MR with PHASER using the VPS29–VPS35C complex (PDB ID code 2R17) as a search model. The crystallographic information is summarized in Table S1.

ITC Assays. ITC experiments were conducted on a VP-ITC microcalorimeter (MicroCal) at 25 °C. Before each experiment, proteins were dialyzed overnight at 4 °C against 50 mM Hepes 7.5, 300 mM NaCl, and 0.5 mM TCEP, and degassed for 5 min in a ThermoVac sample degasser before titration. Each experiment involved one initial 2-μL injection (not used in data fitting), followed by 27 injections of 10-μL aliquots with a spacing of 360 s between injections. Data were analyzed using the Origin ITC software package supplied by MicroCal by fitting a "one set of sites" model to the binding isotherm. For the ITC analysis of the binding between RidL and retromer, 80–110 μM RidL (full-length or $RidL_{30–236}$) was injected into the sample cell containing 9–11 μM of different combinations of retromer subunits (VPS26–VPS29–VPS35, VPS29–VPS35C, or VPS29). The analysis of the interaction between RidL and VPS29 was performed by titrating 100–120 μM of RidL into 10 μM of different VPS29 mutants (Y165A, Y163A, L152E, and VPS26–$VPS29_{Y163A}$–VPS35) or 150 μM $RidL_{\Delta L}$, $RidL_{Y166A}$, or $RidL_{I170D}$ into 10 μM VPS29. For the ITC analysis of the binding between $TBC1D5_{TBC}$ and retromer, 200–220 μM $TBC1d5_{TBC}$ was titrated into 9–12 μM of the different retromer proteins (retromer, VPS26–$VPS29_{Y163A}$–VPS35, VPS29, or the different VPS29 mutants). Finally, the interaction between VARPc and the different retromer proteins was carried out by titrating 140–150 μM into 10 μM of retromer variants. Data are the mean of a minimum of three independent runs for each experiment.

GST-Tagged Pull-Down Experiments. For the identification of the region of RidL that binds to retromer, 20 μM VPS29-[GST-VPS35C] was incubated with 20 μM RidL or different RidL constructs for 1 h at 4 °C in buffer C. Then, 20 μL of equilibrated Glutathione Sepharose beads (GE Healthcare) were added to 70 μL of the protein mixture and incubated for 1 h at 4 °C with gentle agitation. Beads were washed three times with 1 mL buffer C followed by 5 min centrifugation at 3,000 × *g*. Bound proteins were eluted with SDS-containing sample buffer, resolved by SDS/PAGE and visualized by Coomassie blue staining.

Precipitation assays with VPS29 mutants were performed following the same protocol as described above but with the GST-tag present on RidL or $RidL_{\Delta L}$.

Competitive Binding Assay. For the competition assay, preformed complexes were separated by gel-filtration in buffer C to remove excess protein. The purified complexes were incubated with an equimolar amount of RidL, in the

case of the complex formed by $TBC1D5_{TBC}$ and retromer or VARPc and VPS29–VPS35, or $TBC1D5_{TBC}$ or VARPc, in the case of the complex of RidL and retromer. The protein mixtures were once again separated by gel-filtration in buffer E.

Full experimental procedures and associated references can be found in *SI Materials and Methods*.

ACKNOWLEDGMENTS. We thank Ander Vidaurrazaga (Centro de Investigación Cooperativa en Biociencias) for technical assistance and Devanand Bondage (National Institute of Child Health and Human Development) for proliferation assays of *Legionella pneumophila*. This study made use of the Diamond Light Source (Oxfordshire, United Kingdom), the European Synchrotron Radiation Facility (Grenoble, France), and the ALBA synchrotron beamline BL13-XALOC, funded in part by the Horizon 2020 programme of the European Union, iNEXT (H2020 Grant 653706). We thank all the staff from these facilities for technical and human support. This work was supported by the Spanish Ministry of Economy and Competitiveness Grant BFU2014-59759-R (to A.H.); the Severo Ochoa Excellence Accreditation SEV-2016-0644; and the Intramural Program of the Eunice Kennedy Shriver National Institute of Child Health and Human Development (Projects ZIA HD001607 and ZIA HD008893). M.R.-M. is supported by a pre-doctoral fellowship from the Basque Government (PRE_2016_2_0249).

1. Huotari J, Helenius A (2011) Endosome maturation. *EMBO J* 30:3481–3500.
2. Scott CC, Vacca F, Gruenberg J (2014) Endosome maturation, transport and functions. *Semin Cell Dev Biol* 31:2–10.
3. Chi RJ, Harrison MS, Burd CG (2015) Biogenesis of endosome-derived transport carriers. *Cell Mol Life Sci* 72:3441–3455.
4. Hierro A, Gershlick DC, Rojas AL, Bonifacino JS (2015) Formation of tubulovesicular carriers from endosomes and their fusion to the *trans*-Golgi network. *Int Rev Cell Mol Biol* 318:159–202.
5. van Weering JR, Verkade P, Cullen PJ (2010) SNX-BAR proteins in phosphoinositide-mediated, tubular-based endosomal sorting. *Semin Cell Dev Biol* 21:371–380.
6. Burd C, Cullen PJ (2014) Retromer: A master conductor of endosome sorting. *Cold Spring Harb Perspect Biol* 6:a016774.
7. Seaman MN (2012) The retromer complex—Endosomal protein recycling and beyond. *J Cell Sci* 125:4693–4702.
8. Cullen PJ, Korswagen HC (2011) Sorting nexins provide diversity for retromer-dependent trafficking events. *Nat Cell Biol* 14:29–37.
9. Johannes L, Wunder C (2011) The SNXy flavours of endosomal sorting. *Nat Cell Biol* 13:884–886.
10. Lucas M, Hierro A (2017) Retromer. *Curr Biol* 27:R687–R689.
11. Teasdale RD, Collins BM (2012) Insights into the PX (phox-homology) domain and SNX (sorting nexin) protein families: Structures, functions and roles in disease. *Biochem J* 441:39–59.
12. Rojas R, Kametaka S, Haft CR, Bonifacino JS (2007) Interchangeable but essential functions of SNX1 and SNX2 in the association of retromer with endosomes and the trafficking of mannose 6-phosphate receptors. *Mol Cell Biol* 27:1112–1124.
13. Rojas R, et al. (2008) Regulation of retromer recruitment to endosomes by sequential action of Rab5 and Rab7. *J Cell Biol* 183:513–526.
14. Seaman MN, Harbour ME, Tattersall D, Read E, Bright N (2009) Membrane recruitment of the cargo-selective retromer subcomplex is catalysed by the small GTPase Rab7 and inhibited by the Rab-GAP TBC1D5. *J Cell Sci* 122:2371–2382.
15. Harrison MS, et al. (2014) A mechanism for retromer endosomal coat complex assembly with cargo. *Proc Natl Acad Sci USA* 111:267–272.
16. Gomez TS, Billadeau DD (2009) A FAM21-containing WASH complex regulates retromer-dependent sorting. *Dev Cell* 17:699–711.
17. Hesketh GG, et al. (2014) VARP is recruited on to endosomes by direct interaction with retromer, where together they function in export to the cell surface. *Dev Cell* 29: 591–606.
18. Fukuda M (2016) Multiple roles of VARP in endosomal trafficking: Rabs, retromer components and R-SNARE VAMP7 meet on VARP. *Traffic* 17:709–719.
19. Hierro A, et al. (2007) Functional architecture of the retromer cargo-recognition complex. *Nature* 449:1063–1067.
20. Lucas M, et al. (2016) Structural mechanism for cargo recognition by the retromer complex. *Cell* 167:1623–1635.e14.
21. Shi H, Rojas R, Bonifacino JS, Hurley JH (2006) The retromer subunit Vps26 has an arrestin fold and binds Vps35 through its C-terminal domain. *Nat Struct Mol Biol* 13: 540–548.
22. Collins BM, et al. (2008) Structure of Vps26B and mapping of its interaction with the retromer protein complex. *Traffic* 9:366–379.
23. Gallon M, et al. (2014) A unique PDZ domain and arrestin-like fold interaction reveals mechanistic details of endocytic recycling by SNX27-retromer. *Proc Natl Acad Sci USA* 111:E3604–E3613.
24. Clairfeuille T, et al. (2016) A molecular code for endosomal recycling of phosphorylated cargos by the SNX27-retromer complex. *Nat Struct Mol Biol* 23:921–932.
25. Collins BM, Skinner CF, Watson PJ, Seaman MN, Owen DJ (2005) Vps29 has a phosphoesterase fold that acts as a protein interaction scaffold for retromer assembly. *Nat Struct Mol Biol* 12:594–602.
26. Wang D, et al. (2005) Crystal structure of human vacuolar protein sorting protein 29 reveals a phosphodiesterase/nuclease-like fold and two protein-protein interaction sites. *J Biol Chem* 280:22962–22967.
27. Jia D, et al. (2016) Structural and mechanistic insights into regulation of the retromer coat by TBC1d5. *Nat Commun* 7:13305.
28. Personnic N, Bärlocher K, Finsel I, Hilbi H (2016) Subversion of retrograde trafficking by translocated pathogen effectors. *Trends Microbiol* 24:450–462.
29. Groppelli E, Len AC, Granger LA, Jolly C (2014) Retromer regulates HIV-1 envelope glycoprotein trafficking and incorporation into virions. *PLoS Pathog* 10:e1004518.
30. Popa A, et al. (2015) Direct binding of retromer to human papillomavirus type 16 minor capsid protein L2 mediates endosome exit during viral infection. *PLoS Pathog* 11:e1004699.
31. Pim D, Broniarczyk J, Bergant M, Playford MP, Banks L (2015) A novel PDZ domain interaction mediates the binding between human papillomavirus 16 L2 and sorting nexin 27 and modulates virion trafficking. *J Virol* 89:10145–10155.
32. Kingston D, et al. (2011) Inhibition of retromer activity by herpesvirus saimiri tip leads to CD4 downregulation and efficient T cell transformation. *J Virol* 85:10627–10638.
33. Mirrashidi KM, et al. (2015) Global mapping of the Inc-human interactome reveals that retromer restricts *Chlamydia* infection. *Cell Host Microbe* 18:109–121.
34. Paul B, et al. (2017) Structural basis for the hijacking of endosomal sorting nexin proteins by *Chlamydia trachomatis*. *eLife* 6:e22311.
35. Elwell CA, et al. (2017) *Chlamydia* interfere with an interaction between the mannose-6-phosphate receptor and sorting nexins to counteract host restriction. *eLife* 6:e22709.
36. Isberg RR, O'Connor TJ, Heidtman M (2009) The *Legionella pneumophila* replication vacuole: Making a cosy niche inside host cells. *Nat Rev Microbiol* 7:13–24.
37. Horwitz MA (1983) The Legionnaires' disease bacterium (*Legionella pneumophila*) inhibits phagosome-lysosome fusion in human monocytes. *J Exp Med* 158:2108–2126.
38. Horwitz MA (1983) Formation of a novel phagosome by the Legionnaires' disease bacterium (*Legionella pneumophila*) in human monocytes. *J Exp Med* 158:1319–1331.
39. Tilney LG, Harb OS, Connelly PS, Robinson CG, Roy CR (2001) How the parasitic bacterium *Legionella pneumophila* modifies its phagosome and transforms it into rough ER: Implications for conversion of plasma membrane to the ER membrane. *J Cell Sci* 114:4637–4650.
40. Swanson MS, Isberg RR (1995) Association of *Legionella pneumophila* with the macrophage endoplasmic reticulum. *Infect Immun* 63:3609–3620.
41. Ensminger AW (2016) *Legionella pneumophila*, armed to the hilt: Justifying the largest arsenal of effectors in the bacterial world. *Curr Opin Microbiol* 29:74–80.
42. Qiu J, Luo ZQ (2017) *Legionella* and *Coxiella* effectors: Strength in diversity and activity. *Nat Rev Microbiol* 15:591–605.
43. Zusman T, et al. (2007) The response regulator PmrA is a major regulator of the icm/dot type IV secretion system in *Legionella pneumophila* and *Coxiella burnetii*. *Mol Microbiol* 63:1508–1523.
44. Finsel I, et al. (2013) The *Legionella* effector RidL inhibits retrograde trafficking to promote intracellular replication. *Cell Host Microbe* 14:38–50.
45. Holm L, Rosenstrom P (2010) Dali server: Conservation mapping in 3D. *Nucleic Acids Res* 38:W545–W549.
46. Norwood SJ, et al. (2011) Assembly and solution structure of the core retromer protein complex. *Traffic* 12:56–71.
47. Roy S, Leidal AM, Ye J, Ronen SM, Debnath J (2017) Autophagy-dependent shuttling of TBC1D5 controls plasma membrane translocation of GLUT1 and glucose uptake. *Mol Cell* 67:84–95.e5.
48. McNally KE, et al. (2017) Retriever is a multiprotein complex for retromer-independent endosomal cargo recycling. *Nat Cell Biol* 19:1214–1225.
49. Moravcevic K, Oxley CL, Lemmon MA (2012) Conditional peripheral membrane proteins: Facing up to limited specificity. *Structure* 20:15–27.
50. Purushothaman LK, Arlt H, Kuhlee A, Raunser S, Ungermann C (2017) Retromer-driven membrane tubulation separates endosomal recycling from Rab7/Ypt7-dependent fusion. *Mol Biol Cell* 28:783–791.
51. van der Kant R, et al. (2015) Characterization of the mammalian CORVET and HOPS complexes and their modular restructuring for endosome specificity. *J Biol Chem* 290: 30280–30290.
52. Sheffield P, Garrard S, Derewenda Z (1999) Overcoming expression and purification problems of RhoGDI using a family of "parallel" expression vectors. *Protein Expr Purif* 15:34–39.